Contents lists available at ScienceDirect

Chinese Chemical Letters

journal homepage: www.elsevier.com/locate/cclet

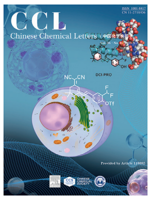

Ultrathin NiS_2 nanocages with hierarchical-flexible walls and rich grain boundaries for efficient oxygen evolution reaction

Chupeng Luo[1], Keying Su[1], Shan Yang, Yujia Liang, Yawen Tang*, Xiaoyu Qiu*

School of Chemistry and Materials Science, Jiangsu Key Laboratory of New Power Batteries, Jiangsu Collaborative Innovation Center of Biomedical Functional Materials, Nanjing Normal University, Nanjing 210023, China

ARTICLE INFO

Article history:
Received 17 December 2023
Revised 6 March 2024
Accepted 28 April 2024
Available online 29 April 2024

Keywords:
Nickel sulfide
Ultrathin nanocages
Grain boundaries
Kinetics control
Oxygen evolution reaction

ABSTRACT

Shape control of nickel sulfide (NiS_2) catalysts is beneficial for boosting their catalytic performances, which is vital to their practical application as a class of advanced non-noble electro-catalysts. However, precisely controlling the formation kinetics and fabricate ultrathin NiS_2 nanostructures still remains challenge. Herein, we provide an injection rate-mediated method to fabricate ultrathin NiS_2 nanocages (HNCs) with hierarchical walls, high-density lattice defects and abundant grain boundaries (GBs). Through mechanism analysis, we find the injection rate determines the concentration of S^{2-} in the steady state and thus control the growth pattern, leading to the formation of NiS_2 HNCs at slow etching kinetics and NiCo PBA@NiS_2 frames at fast etching kinetics, respectively. Benefiting from the ultrathin and hierarchical walls that minimize the mass transport restrictions, the high-density lattice defects and GBs that offer abundant unsaturated reaction sites, the NiS_2 HNCs exhibit obviously enhanced electrocatalytic activity and stability toward OER, with overpotential of 255 mV to reach 10 mA/cm^2 and a Tafel slope of 27.44 mV/dec, surpassing the performances of NiCo PBA@NiS_2 frames and commercial RuO_2.

Electrochemical oxygen evolution reaction (OER) is a key half-reactions in various energy conversion and storage systems, such as rechargeable metal-air batteries, water splitting technique, and nitrogen/carbon dioxide reduction devices [1-6]. To overcome the sluggish four-proton-coupled reaction kinetics and highly oxidative environment of OER, considerable attention is focused on the development of efficient electrocatalysts with expectable activity and stability [7-13]. Up to now, Ir and Ru-based catalysts are the benchmark catalysts for OER, but their scarcity and high cost inevitably limit the large-scale applications [14-17]. Great efforts have been devoted into seeking for low cost and eco-friendly non-precious metal electrocatalysts [18]. Alternatively, pyrite-type nickel sulfides (NiS_2) have emerged as one kind of the promising candidates for alkaline OER due to their high chemical stability and unique structural configuration [19]. The sulfur atoms with high electronegativity can not only modulate the electronic structures of Ni, but also act as proton attachment/detachment sites [20]. Other side, the sulfur atoms in NiS_2 can accelerate the in situ electro-chemical transformation of Ni species into corresponding (oxy) hydroxide active phase, which outperform the pure (oxy) hydroxides in terms of catalytic activity [21-23].

Great efforts have been devoted into further enhancing the OER activity of NiS_2 catalysts, wherein the shape control has been regarded as an effective way due to the follwing reasons: (1) Through designing the geometrical structure of NiS_2, the atom rearrangements may shorten the width of forbidden band, making it easier for electrons to jump from valence band to conduction band, thereby enhancing the conductivity of NiS_2 and guaranteeing the electron transport in electro-catalytic process [24]; (2) The remaining cavities in the valence band after electron transition could tune the adsorption strength towards key intermediates, thereby optimizing the reaction pathway [25]; (3) Through tuning the nanostructured morphology, the density of exposed active sites on the surface of NiS_2 will be increased, and the contact area will be extended for electrolyte access [26-28].

Take above considerations, hollow nanocage structures have attracted comparative attentions due to their large surface-area-to-volume ratios and high-density low-coordinated atoms at the edges, which can enable more active site exposure and faster mass/electron transfer pathway than the solid counterparts [29,30]. On this basis, further producing lattice defects (*i.e.*, vacancy defects, dislocations, and grain boundaries) on hollow nanocage structures could provide more unsaturated coordination sites, and optimize the electronic structure to promote catalytic activity [31,32].

---

* Corresponding authors.
E-mail addresses: tangyawen@njnu.edu.cn (Y. Tang), 07255@njnu.edu.cn (X. Qiu).

[1] These authors contributed equally to this work.

https://doi.org/10.1016/j.cclet.2024.109940

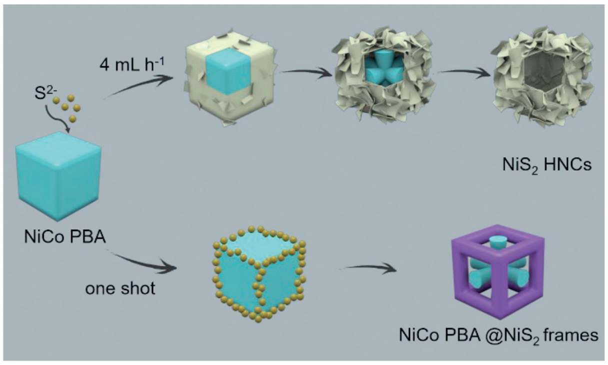

Fig. 1. Schematic illustration for two distinct pathways that generate ultrathin NiS_2 HNCs and NiCo PBA@NiS_2 nanoframes, respectively.

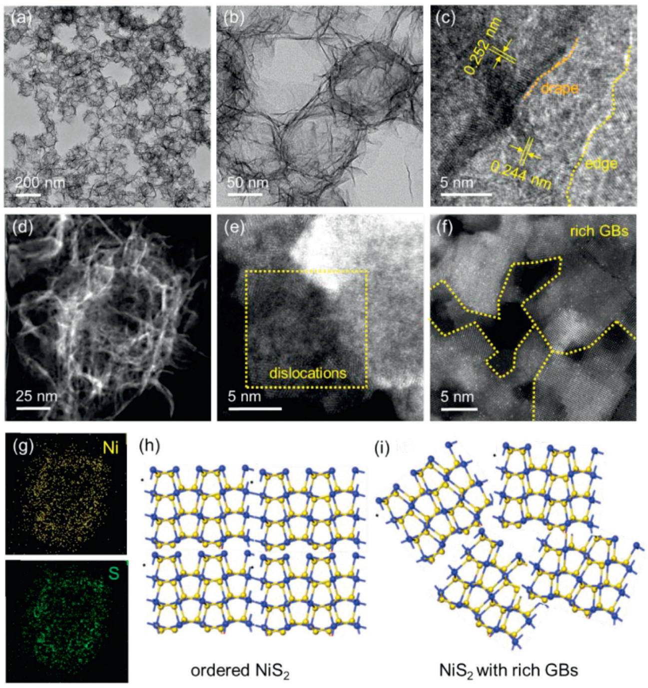

Fig. 2. (a-c) HRTEM images of the ultrathin NiS_2 HNCs. (d-f) HAADF-STEM images of the ultrathin NiS_2 HNCs at different magnifications. (g) Elemental mapping images. (h, i) Structural comparison of the ordered NiS_2 nanocrystals and NiS_2 HNCs.

However, previously reported methods to synthesize hollow NiS_2 nanocages generally involve high-temperature solid-state methods, which are not only energy-intensive but also easy to form bulk NiS_2 cages with thick and rigid walls (normally with thickness of 16.2–46.5 nm) [33-35]. The too thick walls are not only unfavorable for the actives sites exposure and electrolyte penetration, but also hard to produce lattice defects. Unfortunately, in comparison with the shape control of noble-metal catalyst, the formation of NiS_2 is much more thermodynamical unfavored, together with hardly controllable nucleation and growth kinetics. Still now, the exploration of facial and effective method to fabricate hollow NiS_2 nanocages with ultrathin and rich-defects features still remains a grand challenge.

Herein, we developed an injection rate-mediated method to fabricate ultrathin NiS_2 HNCs with hierarchical walls, high-density lattice defects and abundant grain boundaries (GBs). Then, we systematically understood the underlying formation mechanism for the formation of NiS_2 HNCs, wherein the injection rate determined the concentration of S^{2-} in the steady state and thus controlled the growth pattern. At a slow injection rate, the gradually increased number of S^{2-} in the solution was slow enough to initiate the layer-by-layer stripping of NiCo PBA, but fast enough to sustain the cubic structure, thereby forming the ultrathin NiS_2 HNCs. In contrast, one-shot injection led to the high concentration of S^{2-} at the start of the reaction, thereby forming the NiCo PBA@NiS_2 frames at fast kinetic rate. Benefiting from the ultrathin and hierarchical walls that minimize the mass transport restrictions, the high-density lattice defects and GBs that offer abundant unsaturated reaction sites, the as-prepared NiS_2 HNCs can realize efficient electro-catalysis for OER in terms of the high specific activity, favorable kinetics, superior durability, and rapid charge transfer.

Fig. 1 schematically illustrates two distinct pathways that generate ultrathin NiS_2 HNCs and NiCo PBA@NiS_2 nanoframes when the Na_2S precursor was added dropwise and in one shot, respectively. First, face-centered cubic (*fcc*)-structured NiCo PBA nanocubes ($Ni_3[Co(CN)_6]_2$), with transition-metal ions bridged by cyano ligands, were synthesized by a hydrothermal method. Transmission electron microscopy (TEM) image, scanning electron microscopy (SEM) image, and X-ray powder diffraction (XRD) pattern confirm the uniformly cubic shape and high purity phase of $Ni_3[Co(CN)_6]_2$ with average diameter of 93 nm (Fig. S1 in Supporting information). Then, a facile S^{2-} etching method was used to yield ultrathin NiS_2 HNCs. As the equipment photographs (Fig. S2 in Supporting information), a syringe pump was used to precisely control the injection rate of Na_2S at 4.0 mL/h. At such a slow dropwise rate, the low concentration of S^{2-} in the solution led to the layer-by-layer stripping of NiCo PBA nanocubes, thereby forming the ultrathin NiS_2 nanocages with hierarchically flexible walls. Other side, when the Na_2S was added by one shot, the high concentration of S^{2-} in the solution led to the preferentially etching at the edges/corners of the nanocubes with relatively high surface energy, forming the outer NiS_2 nanoframes. Meanwhile, along with the consuming of S^{2-}, the remaining concentration of S^{2-} is too low to etch the total NiCo PBA, leaving the internally residual PBA with eight-corners-cuted cross-like structure, thereby forming the NiCo PBA@NiS_2 nanoframes.

The morphology of the ultrathin NiS_2 HNCs was first analyzed by SEM images (Fig. S3 in Supporting information). The hollow architecture with hierarchical and flexible walls can be discerned unambiguously, signifying that the solid NiCo PBAs nanocubes were all transformed to the hollow-structured NiS_2 nanocages through S^{2-} etching. Large-scale high-resolution TEM (HRTEM) image further unravels the hollow nanocage shape with diameter of 96.2 nm (Fig. 2a). The shell thicknesses measured from the height profile of the randomly selected fragments exhibits an averaging value of *ca.* 3.2 nm, demonstrating the ultrathin nature of NiS_2 HNCs (Fig. 2b and Fig. S4 in Supporting information). The HRTEM images reveal the clear lattice fringes with spacing of 0.252 nm, which is in accordance with the lattice spacing of standar NiS_2 (200) (Fig. 2c). Meanwhile, as marked by orange dashes, clear drapes could be observed, suggesting that the shell of NiS_2 nanocages is consisted of numerous flexible two-dimensional (2D) nanosheet building blocks. These flexible connections are favourable for enhancing the electron and mass transfer in electro-catalysis [36,37]. Atomic-resolution high-angle annular dark-field scanning transmission electron microscopy (HAADF-STEM) was then employed to examine the atomic structure of the ultrathin NiS_2 HNCs (Figs. 2d-f and Fig. S5 in Supporting information). Enlarged from the edge of the hierarchical and flexible shell, the NiS_2 nanocrystals exhibit the disordered and anisotropic lattice orientations. A mass of lattice defects, such as atomic kinks and steps, can be observed from the discontinuous fringes regions, as marked by yellow dash box (Fig. 2e). These may be induced by the S^{2-} etching at a very slow kinetics that disrupts the ordered arrangement of Ni and Co atoms

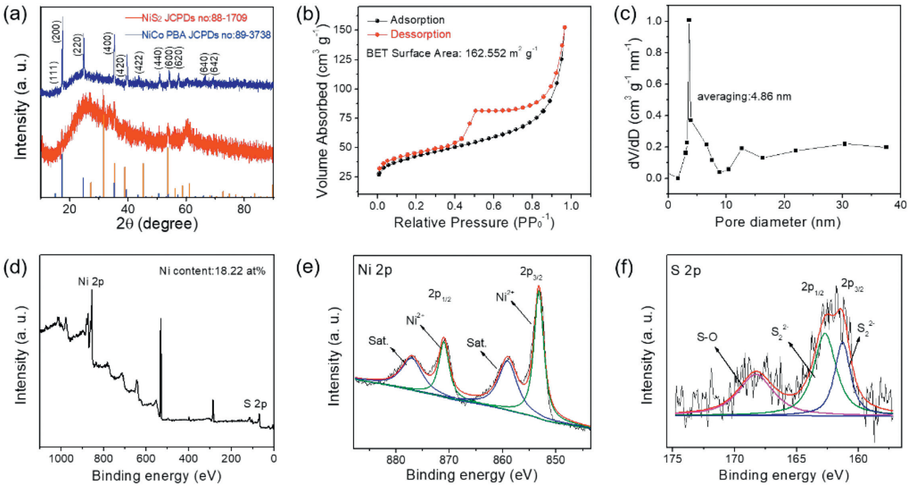

Fig. 3. (a) XRD pattern. (b) Nitrogen absorption-desorption spectra. (c) Pore diameter distribution, XPS spectra at (d) full-range. (e) Ni 2p, and (f) S 2p for the ultrathin NiS_2 HNCs.

in PBA. The further enlarged HAADF-STEM image confirms the existance of rich grain boundaries in NiS_2 HNCs (Fig. 2f). Clear grain boundaries with different atom orientations were catched between two adjacent pieces of NiS_2, indicating that the NiS_2 HNCs are constructed by a crowd of short-range grain boundaries with disordered atom arrangements. The energy-dispersive X-ray (EDX) elemental mapping images reveal a uniform distribution of Ni, S, further confirming the formation of NiS_2 (Fig. 2g). As schematically shown in Fig. 2h, normally, the grain boundary-free NiS_2 exhibites ordered wurtzite structure with Ni^{2+} occupying the octahedral space and S^{2-} occupying the tetrahedral space. In contrast, our NiS_2 with rich grain boundaries indicates highly distorted structures and anisotropic atom orientations (Fig. 2i). Such a unique structure could effectively create more defects, provide accessible active sites, and shorten the mass transport pathway of electrons/ions in electrocatalysis process [38,39]. Other side, by using the same synthetic method expected for adding S^{2-} in one shot, NiCo PBA@NiS_2 frames could be obtained. Large-scale TEM and SEM images indicate the inner 3D cross-like structure with six “arms”, together with outer frame-like structure with six “pillars” (Figs. S6a-e in Supporting information). As evidenced by EDX line scan and mapping images, the inner nanocross is composed of NiCo PBA and the outer frame is composed of nickel-based sulfide, pointing to the NiCo PBA@NiS_2 frames structure (Figs. S6f and g in Supporting information).

The crystal structure of as-prepared ultrathin NiS_2 HNCs were unveiled by XRD pattern, which displays a set of peaks corresponding to the cubic NiS_2 (JCPDS No. 88–1709), indicating the completely phase transformation from NiCo PBA to NiS_2 with well crystallinity (Fig. 3a). N_2 adsorption-desorption isotherms were used to examine the porosity and surface area of the ultrathin NiS_2 HNCs. The Brunauer-Emmett-Teller (BET) surface area measurements show that the NiS_2 HNCs possess a large specific surface area of 162.56 m^2/g, which could be ascribed to the existence of layer-by-layer stripped ultrathin shells in NiS_2 nanocages (Fig. 3b). Pore diameter distribution exhibits an average pore size of 4.86 nm for the NiS_2 HNCs (Fig. 3c). As revealed the morphology analysis in Fig. 2, numerous atomic steps/kinks and abundant grain boundaries are formed on the surface of NiS_2 nanocages, which may make contribution to the mesopores formation. The surface composition were probed by the X-ray photoelectron spectroscopy (XPS) technology. As the whole XPS survey shown in Fig. 3d, clear characteristic peaks corresponding to Ni and S elements could be detected. Meanwhile, the Ni content was measured to be 18.22 at%, which was similar to the result determined by inductively coupled plasma optical emission spectrometry (ICP-OES, 19.58 at%). For high resolution Ni 2p spectra, the peaks at 870.8 and 852.9 eV are attributed to the oxidation state of Ni $2p_{1/2}$ and Ni $2p_{3/2}$ energy level in NiS_2. Meanwhile, the peaks at 879.4 and 861.4 eV are corresponding to the satellites of Ni $2p_{1/2}$ and Ni $2p_{3/2}$ energy level, respectively (Fig. 3e) [40]. For high resolution S 2p spectra, three distinct peaks located at 161.4, 162.5, and 168.3 eV can be deconvoluted, attributing to the S $2p_{3/2}$ and S $2p_{1/2}$ and the S-O bond (superficial oxidation of NiS_2), respectively (Fig. 3f) [41,42].

For better understanding the formation mechanism of the ultrathin NiS_2 HNCs, the influences of etching agent and NiCo PBA nanocubes were taken into consideration. As the TEM images shown in Fig. S7 (Supporting information), products prepared by using 2 mL of Na_2S solution displayed the solid sphere structure surrounding by a small amount of lamellar nanosheets, indicating the insufficient etching of the NiCo PBA nanocubes. While increasing the volume of Na_2S solution to 6 mL and 8 mL, the products exhibited an irregular shape with randomly dispersed spheres and nanosheets, indicating the uncontrolled etching kinetics when the volume of Na_2S was excessive. Other side, the diameter of NiCo PBA nanocubes was found to influence the formation of ultrathin NiS_2 HNCs. As the TEM images shown in Fig. S8 (Supporting information), products prepared by using the large-sized NiCo PBA nanocubes exhibited the solid structure with rough surfaces, pointing to the insufficient S^{2-} etching on large-sized NiCo PBA nanocubes. When increasing the volume of Na_2S solution to 12 mL, the products exhibited the hollow nanocage structure with diameter of ca. 300 nm, indicating the well transformation from NiCo PBA to NiS_2 nanocages (Fig. S8b). This result indicates that the large-sized NiCo PBA nanocubes could also be used to fabricate the NiS_2 nanocages, but the amount of etching agent should be increased.

Since the injection rate directly influences the growth pattern, TEM images acquired at a wide range of injection rates were revealed to show detailed structural changes. As shown in Fig. S9 (Supporting information), products obtained at a fast injection rate of 6 mL/h exhibited an irregular shape with sphere-like NiCo PBA and randomly dispersed NiS_2 flexible nanosheets, indicating the incomplete etching of NiCo PBA at a too fast injection rate. In contrast, the products obtained at 3 and 2 mL/h exhibited a major hierarchical flower-like structure with hard observation of any cage-like structure. This result implies that further slowing down the injection rate will decrease the NiS_2 stripping rate, thus the hollow cage structure was hard to be maintained (Figs. S9b and c). Therefore, 4 mL/h could be the optimal injection rate to obtain the

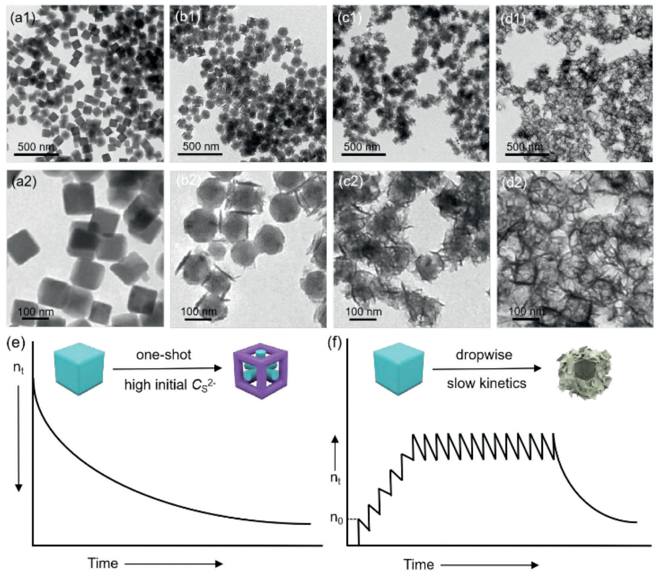

Fig. 4. Time-dependent TEM images for the ultrathin NiS_2 HNCs recorded at (a) 0 min, (b) 15 min, (c) 30 min, and (d) 60 min. (e, f) Schematic showing the dependence of growth pattern on the injection rate of S^{2-}.

ultrathin NiS_2 HNCs. To investigate the kinetics-conducted etching mechanism at 4 mL/h, intermediates collected at different reaction time were investigated by TEM images (Figs. 4a-d). TEM images taken at the start of the etching displayed the solid cubic structure corresponding to NiCo PBA (Fig. 4a). While TEM images taken at $t = 15$ min displayed the cubic NiCo PBA with rounded corners, together with a small amount of lamellar structure around the NiCo PBA, suggesting the occurrence of the S^{2-} etching (Fig. 4b). The TEM images collected at $t = 30$ min showed an obviously increased number of flexible NiS_2 nanosheets, together with the loss of NiCo PBA cores, indicating the inwards stripping from the outside wall of NiCo PBA nanocubes (Fig. 4c). When the injection time was prolonged to 1 h, the inner NiCo PBA was etched completely, ultimately ripening into ultrathin NiS_2 HNCs with abundant grain boundaries (Fig. 4d). Based on the above experimental results, a simple injection rate-mediated etching mechanism was proposed. As illustrated in Figs. 4e and f, the injection rate determines the number of S^{2-} in the steady state and thus controls the growth pattern. When the S^{2-} was injected at 4 mL/h, the number of S^{2-} in the solution was gradually increasing along with the time proceeding. The continuous supplement of S^{2-} led to a kinetic rate that slow enough to initiate the layer-by-layer stripping of NiCo PBA, but fast enough to sustain the cubic structure, thereby forming the NiS_2 HNCs. In contrast, when the S^{2-} was injected in one-shot, the number of S^{2-} in the solution reached the maximum amount at the start of the reaction, then the S^{2-} were reacted with NiCo PBA and gradually consumed along with the time proceeding. Until the number of S^{2-} in the solution was insufficient to drive the etching, the reduction was terminated, thus forming the NiCo PBA@NiS_2 nanoframe at a relatively fast kinetic rate.

The OER performances of the ultrathin NiS_2 HNCs were thoroughly appraised in 1.0 mol/L KOH electrolyte, using the standard three-electrode system and in comparison with commercial RuO_2. In order to unveil the effects on electrocatalytic performance brought by the ultrathin and hierarchical structure, the catalytic activity of NiCo PBA@NiS_2 frames was taken into comparison. All potentials hereafter have been *iR*-corrected and referenced to a reversible hydrogen electrode. Fig. 5a presents the linear sweep voltammetry (LSV) curves of all three samples. To reach the current density of 10 mA/cm^2, the overpotential of NiS_2 HNCs is 255 mV, outperforming that of NiCo PBA@NiS_2 frames (304 mV) and RuO_2 (342 mV). Furthermore, it required 334 mV to provide 30 mA/cm^2, much lower than that of the NiCo PBA@NiS_2 frames (431 mV) and RuO_2 (561 mV), as the histograms listed in Fig. 5b. Therefore, we could conclude that the ultrathin and rich-GB features impart nickel sulfide higher intrinsic activity for OER. In addition, to reach the overpotential of 300 mV, the current density for NiS_2 HNCs could reach 35.7 A/g, which is much larger than that for NiCo PBA@NiS_2 frame (16.8 A/g) and RuO_2 (10.2 A/g), indicating the highest specific current density per geometric surface area for NiS_2 HNCs (Fig. 5c). Furthermore, as the histogram shown in Fig. S10 (Supporting information), the turnover frequency (TOF) value for NiS_2 HNCs (16.82 s^{-1}) is much higher than that of the NiCo PBA@NiS_2 frames (7.48 s^{-1}) and RuO_2 (4.23 s^{-1}), suggesting the superior OER intrinsic activity of NiS_2 HNCs. Tafel slopes for NiS_2 HNCs, NiCo PBA@NiS_2 frames and RuO_2 were fitted to be 27.44, 36.13, and 88.17 mV/dec, respectively, indicating the fastest OER kinetics for NiS_2 HNCs (Fig. 5d). Moreover, the superior OER performance of NiS_2 HNCs also surpasses most of the reported values in the literatures, as listed in Table S1 (Supporting information). The double-layer capacitances (C_{dl}) were performed to compare the electrocatalytic active surface areas (ECSAs) of the NiS_2 HNCs and NiCo PBA@NiS_2 frame. Calculated from the cyclic voltammetries at different scan rates (CVs, Fig. S11 in Supporting information), the C_{dl} for NiS_2 HNCs (22.56 mF/cm^2) is much higher than that for NiCo PBA@NiS_2 frame (13.82 mF/cm^2, Fig. 5e). This result suggests that more active sites are exposed on NiS_2 HNCs, and consequently lead to higher catalytic activity for OER. Electrochemical impedance spectroscopy (EIS) measurements were carried out to evaluate the charge transfer ability (Fig. 5f). The NiS_2 HNCs exhibit a much smaller R_{ct} value of 155.4 Ω compared with that of NiCo PBA@NiS_2 nanoframe (245.0 Ω), suggesting the faster charge transfer rate and reaction kinetics for NiS_2 HNCs under the same condition.

The electro-catalytic stability of the NiS_2 HNCs was detected by accelerated durability tests (ADTs) and chronoamperometric measurements. The LSV polarization curves for NiS_2 HNCs were overlapped very well before and after 3000 CV cycles (Fig. 5g). In contrast, the LSV polarization curve of commercial RuO_2 catalyst exhibits an obvious decay in both the overpotential and current density after 3000 cycles, which is inferior to that of the NiS_2 HNCs. (Fig. S12 in Supporting information). Moreover, chronoamperometric measurements illustrate that for the NiS_2 HNCs, the current density achieved at a static potential of 1.55 V only decreases about 11.7% after 12 h (Fig. 5h). In contrast, the NiCo PBA@NiS_2 frames and commercial RuO_2 show obvious decay in current density, with decrements of 13.5% and 35.8%, respectively, further confirming the much better OER stability for NiS_2 HNCs (Fig. S13 in Supporting information). In alkaline media-based OER, transition metal sulfide could be transformed into oxyhydroxides/oxide on the surface, which are effective species to boost OER performance [43,44]. As revealed in Fig. S14 (Supporting information), the Ni 2p XPS spectrum for NiS_2 HNCs after OER deliver two characteristic peaks at 855.9 and 873.5 eV, which are assigned to nickel oxide, demonstrating that Ni species were oxidized during the OER. Besides, the signal of S 2p spectra after the OER was hard to be detected, illustrating the leaching and oxidation of S during electrochemical process. Despite the phase transformation, the NiS_2 HNCs still exhibit the ultrathin and hierarchical nanocage-like structure without obvious morphology change, as confirmed by TEM image (Fig. S15 in Supporting information). Overall, above results clearly demonstrate that constructing ultrathin and hierarchical nanocage structure can effectively enhance the OER activity of NiS_2 catalysts, which might be attributed to the following aspects: (1) The hollow and ultrathin NiS_2 nanocages led to atomtic rearrangements, which may enhance the conductivity and improve the charge transfer capability during

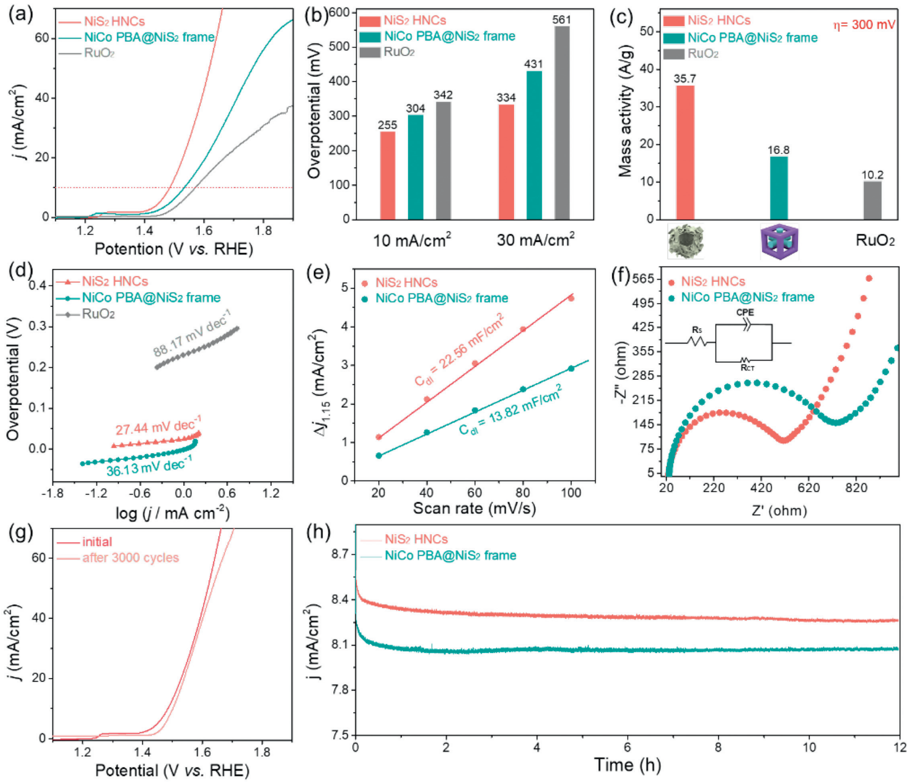

Fig. 5. Electrocatalytic OER performances of the NiS_2 HNCs in 1.0 mol/L KOH electrolyte. (a) LSV polarization curves. (b) Overpotentials at current density of 10 and 30 mA/cm^2, respectively. (c) Current density at $\eta = 300$ mV. (d) Tafel plots. (e) Estimated C_{dl} values. (f) Nyquist plots measured at 1.42 V. (g) LSV polarization curves before and after 3000 cycles. (h) Chronopotentiometry curve performed at 1.55 V.

OER [45,46]; (2) The inter-connected flexible walls could not only minimize mass transport restrictions and facilitate rapid diffusion of reactant molecules, but also provide large contact area for electrolyte access and O_2 release [47-49]; (3) The layer-by-layer stripping of NiCo PBA under a slow etching rate led to the formation of abundant lattice and GB defects, which could serve as additional catalytic sites with high intrinsic activity [50].

In summary, we developed a novel approach to preciously controlling the chemical etching kinetics, *in-situ* transforming NiCo PBA into ultrathin NiS_2 HNCs with rich defects. More importantly, a deep understanding of the underlying formation mechanism for NiS_2 HNCs was provided, wherein the injection rate determined the concentration of S^{2-} in the steady state and thus controlled the growth pattern. Experimental data revealed that such a nanocage-like NiS_2 with ultrathin and hierarchical walls could expose high-density lattice defects and GBs to offer abundant unsaturated reaction sites, and provide interconnected walls to minimize the mass transport restrictions, thereby responsible for optimized intrinsic activity and stability for OER. This work offers new insights into the shape control of non-precious metal-based electrocatalysts, which is promising for developing efficient, cost-effective, and durable electrode materials in energy conversion devices.

Declaration of competing interest

The authors declare that they have no known competing financial interests or personal relationships that could have appeared to influence the work reported in this paper.

Acknowledgments

This work was financially supported by National Natural Science Foundation of China (Nos. 21902078, 22279062, 22232004, 22072067). The authors are grateful for the supports from National and Local Joint Engineering Research Center of Biomedical Functional Materials and a project sponsored by the Priority Academic Program Development of Jiangsu Higher Education Institutions.

Supplementary materials

Supplementary material associated with this article can be found, in the online version, at doi:10.1016/j.cclet.2024.109940.

References

[1] J. Mefford, A. Akbashev, M. Kang, et al., Nature 593 (2021) 67–73.
[2] X. Wang, S. Xi, P. Huang, et al., Nature 611 (2022) 702–708.
[3] L. Chong, G. Gao, J. Wen, et al., Science 380 (2023) 609–616.
[4] W. Kang, R. Wei, H. Yin, et al., J. Am. Chem. Soc. 145 (2023) 3470–3477.
[5] W. Wu, K. Yue, K. Zhang, et al., Energy Lab. 1 (2023) 220020.
[6] M. Li, M. Song, W. Ni, et al., Chin. Chem. Lett. 34 (2023) 107571.
[7] Y. Wang, Y. Zhao, L. Liu, et al., J. Am. Chem. Soc. 145 (2023) 20261–20272.
[8] J. Geppert, P. Röse, S. Czioska, et al., J. Am. Chem. Soc. 144 (2022) 13205–13217.
[9] X. Xu, S. Wang, S. Guo, et al., Adv. Powder Mater. 1 (2022) 100027.
[10] L. Zeng, J. Zhu, P.K. Chu, et al., Adv. Mater. 34 (2022) 2204636.
[11] L. Lv, B. Tang, Q. Ji, et al., Chin. Chem. Lett. 34 (2023) 107524.
[12] P. Wang, Y. Wang, Z. Shi, et al., Energy Lab. 1 (2023) 220018.
[13] M. Li, L. Feng, Chin. J. Struct. Chem. 41 (2022) 2201019–2201024.
[14] D. Escalera-López, S. Czioska, J. Geppert, et al., ACS Catal. 11 (2021) 9300–9316.
[15] W. Zhu, X. Song, F. Liao, et al., Nat. Commun. 14 (2023) 5365.
[16] J. Yang, Y. Shen, Y. Sun, et al., Angew. Chem. Int. Ed. 62 (2023) e202302220.
[17] J. Yin, J. Jin, M. Lu, et al., J. Am. Chem. Soc. 142 (2020) 18378–18386.
[18] L. Yang, W. Hong, Y. Zhang, et al., Adv. Funct. Mater. 29 (2019) 1903454.
[19] L. Zhang, J. Rong, Y. Yang, et al., Small 19 (2023) 2207472.
[20] C. Karakaya, N. Solati, U. Savacı, et al., ACS Catal. 10 (2020) 15114–15122.
[21] W. Cheng, S. Xi, Z. Wu, D. Luan, X. Lou, Sci. Adv. 7 (2021) eabk0919.
[22] R. Zeng, Y. Yang, X. Feng, et al., Sci. Adv. 8 (2022) eabj1584.
[23] C. Liu, F. Yang, A. Schechter, L. Feng, Adv. Sens. Energy Mater. 2 (2023) 100055.
[24] S. Zhou, X. Jin, S. Zhu, et al., Chin. Chem. Lett. 31 (2020) 2353–2357.
[25] M. Zhao, Y. Gu, W. Gao, et al., Appl. Catal. B 266 (2020) 118625.
[26] S. Xiao, J. Jiang, Y. Zhu, et al., Adv. Powder Mater. 2 (2023) 100120.
[27] X. Lin, J. Liu, X. Qiu, et al., Angew. Chem. Int. Ed. 62 (2023) e202306333.
[28] S. Sk, R. Madhu, D.S. Gavali, et al., J. Mater. Chem. A 11 (2023) 10309–10318.

[29] Y. Yang, Y. Kang, H. Zhao, et al., Small 16 (2020) 1905083.
[30] X. Huang, R. Wang, L. Wu, H. Zhang, J. Liu, Small 19 (2023) 2304165.
[31] J. Zhu, Z. Chen, M. Xie, et al., Angew. Chem. Int. Ed. 58 (2019) 7244–7248.
[32] H. Xu, J. Cao, C. Shan, et al., Angew. Chem. Int. Ed. 57 (2018) 8654–8658.
[33] J. Wang, A. Yang, J. Li, et al., Appl. Catal. B 300 (2022) 120727.
[34] J. Wang, A.D. Handoko, Y. Bai, et al., Nano Lett. 22 (2022) 10184–10191.
[35] Z. Cai, Z. Peng, X. Liu, et al., Chin. Chem. Lett. 32 (2021) 3607–3612.
[36] J. Chen, L. Zhang, J. Li, et al., J. Mater. Chem. A 11 (2023) 1116–1122.
[37] Q. Chen, S. Sun, T. Zhai, et al., Adv. Energy Mater. 8 (2018) 1800054.
[38] P. Wang, T. Wang, R. Qin, et al., Adv. Energy Mater. 12 (2022) 2103359.
[39] T. Liu, P. Diao, Z. Lin, H. Wang, Nano Energy 74 (2020) 104787.
[40] W. Shen, Y. Zheng, Y. Hu, et al., J. Am. Chem. Soc. 146 (2024) 5324–5332.
[41] X. Chen, T. Huang, D.H. Kuo, et al., Appl. Catal. B 298 (2021) 120542.
[42] X. Dai, G. Lv, Z. Wu, et al., Adv. Energy Mater. 13 (2023) 2300452.
[43] X. Wang, W. Li, D. Xiong, D.Y. Petrovykh, L. Liu, Adv. Funct. Mater. 26 (2016) 4067–4077.
[44] Q. Li, Small 17 (2021) 2101617.
[45] Y.C. Zhang, C. Han, J. Gao, et al., ACS Catal. 11 (2021) 12485–12509.
[46] X. Lv, X. Li, C. Yang, et al., Adv. Funct. Mater. 30 (2020) 1910830.
[47] R.M. Kluge, E. Psaltis, R.W. Haid, et al., ACS Appl. Mater. Interfaces 14 (2022) 19604–19613.
[48] Z. Ge, T. Wang, Y. Ding, et al., Adv. Energy Mater. 12 (2022) 2103916.
[49] J. Zhu, Z. Gong, C. Yang, Q. Yan, J. Am. Chem. Soc. 143 (2021) 20183–20191.
[50] X. Hai, S. Xi, S. Mitchell, et al., Nat. Nanotechnol. 17 (2022) 174–181.